Boron-Rich Molybdenum Boride with Unusual Short-Range Vacancy Ordering, Anisotropic Hardness, and Superconductivity

Hu Tang,[†,■] Xiang Gao,[†,■] Jian Zhang,[‡,■] Bo Gao,[†] Wenju Zhou,[†,‡] Bingmin Yan,[†] Xue Li,[§] Qinghua Zhang,[∥] Shang Peng,[⊥] Dajian Huang,[†] Lijun Zhang,[#] Xiaohong Yuan,[†] Biao Wan,[#] Chong Peng,[#] Lailei Wu,[#] Dongzhou Zhang,[@] Hanyu Liu,[§] Lin Gu,[∥] Faming Gao,[∇] Tetsuo Irifune,[●] Rajeev Ahuja,[○] Ho-Kwang Mao,[†] and Huiyang Gou[*,†]

HPSTAR
904-2020

[†]Center for High Pressure Science and Technology Advanced Research, Beijing 100094, China

[‡]State Key Laboratory of Crystal Materials, Shandong University, Jinan 250100, China

[§]State Key Laboratory of Superhard Materials & Innovation Center for Computational Physics Methods and Software, College of Physics, Jilin University, Changchun 130012, China

[∥]Beijing National Laboratory for Condensed Matter and Institute of Physics, Chinese Academy of Sciences, Beijing 100190, China

[⊥]School of Physics and Technology, Wuhan University, Wuhan 430072, China

[#]Key Laboratory of Metastable Materials Science and Technology, College of Material Science and Engineering, Yanshan University, Qinhuangdao 066004, China

[@]Hawai'i Institute of Geophysics and Planetology, School of Ocean and Earth Science and Technology, University of Hawai'i at Manoa, Honolulu, Hawaii 96822, United States
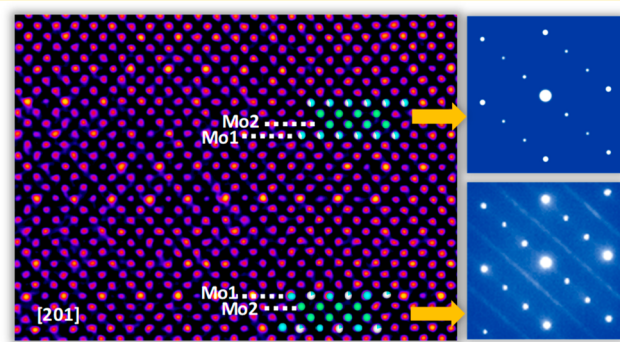
[∇]Key Laboratory of Applied Chemistry, College of Environmental and Chemical Engineering, Yanshan University, Qinhuangdao 066004, China

[●]Geodynamics Research Center, Ehime University, Matsuyama 790-8577, Japan

[○]Condensed Matter Theory Group, Materials Theory Division, Department of Physics & Astronomy, Uppsala University, 75120 Uppsala, Sweden

S *Supporting Information*

ABSTRACT: Determination of the structures of materials involving more light elements such as boron-rich compounds is challenging and technically important in understanding their varied compositions and superior functionalities. Here we resolve the long-standing uncertainties in structure and composition about the highest boride (termed MoB_4, $Mo_{1-x}B_3$, or MoB_3) through the rapid formation of large-sized boron-rich molybdenum boride under pressure. Using high-quality single-crystal X-ray diffraction analysis and aberration-corrected scanning transmission electron microscopy, we reveal that boron-rich molybdenum boride with a composition of $Mo_{0.757}B_3$ exhibits $P6_3/mmc$ symmetry with a partial occupancy of 0.514 in $2b$ Mo sites (Mo1), and direct observations reveal the short-range ordering of cation vacancies in (010) crystal planes. Large anisotropic Young's moduli and Vickers hardness are seen for $Mo_{0.757}B_3$, which may be attributed by its two-dimensional boron distributions. $Mo_{0.757}B_3$ is also found to be superconducting with a transition temperature (T_c) of ∼2.4 K, which was confirmed by measurements of resistivity and magnetic susceptibility. Theoretical calculations suggest that the partial occupancy of Mo atoms plays a crucial role in the emergence of superconductivity.

INTRODUCTION

Boron-rich compounds make up an important class of functional materials with intriguing physicochemical properties such as chemical inertness, high thermal stability, high hardness, superconductivity, and the ability to be semiconducting, thermoelectric, and catalytic.[1−10] In these compounds, the electron-deficient boron is readily bonded

with the guest atoms to form diverse complex structures. Fundamentally, understanding the precise structures and compositions of boron-rich compounds is quite important,

because the structural parameters provide the direct basis for understanding the synthesis and growth mechanism, phase evolution and development, chemical bonding, and functionalities. However, the structural and compositional determinations of boron-rich materials are quite challenging, although extensive efforts and significant progress have been made.[4,11−17]

Boron-rich molybdenum and tungsten borides are very promising candidates for superhard materials in transition metal and light element systems.[2,4,5,7,8,18,19] Despite enormous theoretical and experimental efforts devoted to understanding the exact composition and physical properties, the standard methods, e.g., powder X-ray diffraction (PXRD) and energy-dispersive spectroscopy (EDS), become incapable of complete characterization of the structure and composition due to the involvement of more light elements of boron and the large difference between Mo or W and B atoms. Recently, single-crystal crystallographic analysis of boron-rich tungsten borides reveals a real composition of $W_{1−y}B_{3+x}$ ($y \approx 0.17$, $x \approx 0.5$, $WB_{4.2}$) with partial occupancy of W2 at Wyckoff $2b$ sites and B2 at $6h$ site (in addition, W1 at the $2c$ site and B1 at $12i$ sites).[4] Interestingly, the presence of boron trimers located in the partially filled tungsten sites, forming the cuboctahedral boron cages, could enhance the mechanical property due to the enhanced covalent interaction with boron layers in this highest boride $W_{1−y}B_{3+x}$. The proposed structural solution not only resolves the long-standing discrepancy in the W−B system but also provides a clear picture for our understanding of the physical properties of this boron-rich tungsten boride, such as hardness and superconductivity.

Naturally, boron-rich molybdenum borides are expected to follow the regularity of congeners of chemical elements and their compounds. On the boron-rich side of the Mo−B system, two possible stoichiometries of Mo_2B_5 and MoB_4 have previously been reported.[14,17,20−22] Mo_2B_5 was later found to be Mo_2B_4 with the same $R\bar{3}m$ symmetry using neutron diffraction and single-crystal X-ray diffraction (SC-XRD), but there has been no further report to verify this scenario.[12,16,23,24] For the highest molybdenum boride, the possible structural models with stoichiometric MoB_4 and nonstoichiometric $Mo_{0.8}B_3$, $Mo_{0.91}B_3$, $Mo_{3.46}B_{12}$, $Mo_{1.83}B_9$, and $Mo_{1.094}B_{4.714}$ were proposed previously (listed in Table S1).[4,14,15,25] Among them, MoB_4 with $P6_3/mmc$ symmetry was proposed by theoretical calculations.[14] The structural model of $Mo_{0.8}B_3$ determined by powder diffraction, the electron microprobe, and chemical analysis was often followed for almost half a century,[15] which is derived from two similar structures of $Mo_{0.91}B_3$ and $Mo_{3.46}B_{12}$ by changing the occupancy of Mo at $2b$ sites. Molybdenum and tungsten borides have highly similar crystal structures; therefore, the structural models of tungsten boride were also used for the highest molybdenum boride. $Mo_{1.83}B_9$ and $Mo_{1.094}B_{4.714}$ were derived from the highest boron W−B models proposed by Nowotny et al.[25] and Lech et al.[4] Because of the similar stacking sequence of Mo atoms in these models, the standard PXRD profiles cannot give the direct structural solution. Since then, the structural and compositional uncertainty for this highest boride of molybdenum has been put aside due to the lack of high-quality single-crystal and advanced structural characterization, and also a full depiction of physical and chemical performances remains unexplored in experiment, although it has been proposed to be a potentially superhard and catalytic material. We rationalize that the off-stoichiometry in the highest borides of

molybdenum and tungsten always leads to the multiphase in the reaction products and complicates the interpretation of data. From a synthesis perspective, the severe phase competition restricts the atomic motion during the reaction and slows the grain growth of the individual boride. Theoretically, the structural disorder in the highest borides also prevents computational investigations using first-principles calculations, which usually deal with the regular, ordering structures. The disordered arrangement in the highest boride may strongly affect the rigidity of molybdenum borides, which has not yet been addressed well. Therefore, the sufficient high-quality single crystals and feasible performance characterizations may be a better solution for resolving the uncertainties that have existed for almost half a century.

In this work, by adding metal Pt or Bi flux and delicately manipulating the temperature at high pressures, we have successfully prepared the large single-crystal molybdenum triboride and determined its structure, which unravels Mo atoms with partial occupancy and precise local composition determination in the boron light element. We also achieved high-quality atomic-resolution STEM (scanning transmission electron microscopy) images for boron-rich molybdenum borides by employing spherical aberration-corrected STEM, which reveals short-range ordering of cation vacancies in the (010) crystal planes. The mechanical properties and superconductivity are also evaluated for the first time.

■ EXPERIMENTAL SECTION

Synthesis of Molybdenum Borides at High Temperatures and High Pressures. High-purity crystalline B[11] (200 mesh) and Mo powder (∼1−5 μm) were used as the raw materials. The starting Mo:B atomic ratio is 1:6; in addition, 0.5 mol of metal Pt or Bi powders is added for synthesizing large Mo−B crystals. High-pressure and high-temperature (HPHT) experiments were carried out using a split-cylinder type apparatus (ORANGE-1000) with a designed COMPRES 10/4 assembly (shown in Figure S1a). To distinguish the reaction products from the sample chamber, we deliberately designed an asymmetric assembly with a significant temperature gradient. The low-melting point reaction products eventually flow to the high-temperature area. The pressure was set at 15 GPa and previously calibrated at room temperature using the diagnostic changes in the electrical resistances of ZnTe (9.6 and 12.0 GPa), ZnS (15.5 GPa), GaAs (18.3 GPa), and GaP (23.0 GPa). Temperatures were measured with W−Re (type C) thermocouples. Figure S1b presents two different heating routes. The samples were first heated to the highest target temperatures of 1650 °C (in route 1) and 1750 °C (in route 2) at a rate of 100 °C/min. The temperatures were maintained for 20 min, decreased to 1450 °C at a rate of 10 °C/min, and then held for 40 min. Finally, the samples were cooled to room temperature at a rate of 100 °C/min. Larger samples were prepared by using a CS-1B type hexahedron anvil press with a similar asymmetric assembly (shown in Figure S2a). The applied pressure was 5 GPa, and the heating route is presented in Figure S2b.

Morphology and Structure Analysis. *Scanning Electron Microscope (SEM).* The recovered samples were polished in the radial direction for microstructure analysis. The analysis was carried out by using a field emission SEM (JEOL, JSM-7000F) with an acceleration voltage of 20 kV. Electron back-scatter diffraction (EBSD) was used to distinguish the phase distributions for the recovered samples.

Single-Crystal X-ray Diffraction. A crystal with dimensions of 0.023 mm × 0.013 mm × 0.029 mm was selected and mounted on MiTeGen loops. Single-crystal X-ray diffraction was performed at 293 K using a Bruker D8 Venture diffractometer equipped with a PHOTON 200 area detector. Data were integrated and corrected for oblique incidence with the software package SAINT integrated in the program APEX3. Absorption correction was applied by using the

program SADABS. The crystal structure was determined by the charge flipping algorithm using the program Superflip and then refined by using the program JANA2006.[26] All atoms are refined with anisotropic temperature displacement parameters.

Scanning Transmission Electron Microscope. The cross sectional specimen for XRD and STEM observations was prepared by dual-beam focused ion beam scanning microscopy (Versa 3D, Thermo Fisher) using a Ga ion accelerating voltage ranging from 2 to 40 kV, followed by ion milling (Gatan 691, Gatan) operated from 1.5 to 0.5 kV, and cooled with liquid nitrogen and then argon plasma cleaning (Solarus 950, Gatan) to remove residual amorphous film. A 200 kV ARM-200F (JEOL Ltd.) microscope equipped with a spherical aberration corrector (CEOS GmbH), enabling structures to be probed with subangstrom resolution, was utilized for STEM imaging. A convergence angle of 30 mrad and an annular inner detector angle of ≥70 mrad were chosen for HAADF imaging. EELS analysis was performed using the same convergence angle. Dual-EELS spectra were recorded by scanning a relatively large area in STEM mode.

Measurement of Properties. *In Situ High-Pressure Characterizations.* A high pressure was generated in a symmetrical diamond anvil cell (DAC) with a 300 μm culet. The samples and a ruby sphere (for pressure calibration) were loaded into the sample chamber (120 μm in diameter) in the preindented rhenium gasket, with neon pressure medium. The *in situ* high-pressure XRD patterns with a wavelength of 0.4337 Å were collected at 13-BMC of the Advanced Phonon Source (APS), Argonne National Laboratory (ANL).[27] The compression and decompression experiments were conducted at room temperature. The two-dimensional diffraction patterns were integrated into a one-dimensional profile with the Dioptas program.[28] Structural refinements were performed with the GSAS program.[29]

Mechanical Properties. A Hysitron Triboindenter (TI-900) having *in situ* AFM and a Berkovich diamond tip with an effective tip radius of 450 nm was used for nanoindentation measurements of synthesized Mo−B compounds. The samples were uploaded to the maximum load of 9000 μN at a loading rate of 1000 μN s^{-1} with a holding time of 2 s, followed by a decrease to zero to measure the hardness and elastic modulus on different samples. The thermal drift was maintained below 0.05 nm/s during the test process. The hardness of Mo−B samples was also evaluated by a micro-Vickers hardness tester (FM-700, Future-Tech). Vickers hardness values were measured using a Vickers diamond indenter with a load of 0.01−1.96 N and a holding time of 10 s. H_v was determined from the equation

$$H_v = \frac{1854.4F}{L^2} \tag{1}$$

where F (newtons) is the applied load and L (micrometers) is the arithmetic mean of the two diagonals of the Vickers indentation.

Superconductivity Measurement. The electrical resistance and magnetic susceptibility measurements were performed on the physical property measurement system (Quantum Design, PPMS). The electrical resistance was collected at temperatures of 1.8−300 K, and the magnetic property was measured under an applied field of 10 Oe with zero-field-cooling and field-cooling protocols.

Theoretical Simulations. $Mo_{0.757}B_3$ with an average occupancy in Mo1 sites based on SC-XRD data was used as the initial structure for calculating the elastic constants and the superconducting transition temperature. Structural optimizations were performed using density functional theory as implemented in the Quantum-ESPRESSO package.[30] The electron−phonon coupling (EPC) calculations were simulated within the framework of linear response theory through the Quantum-ESPRESSO code.[30] Among the whole calculations, the ultrasoft pseudopotentials were selected with a kinetic energy cutoff of 65 Ry and a *q* grid of 4 × 4 × 4 in reciprocal space. *K* grids of 8 × 8 × 8 were adopted to ensure *k*-point sampling convergence with a Gaussian broadening width of 0.02 Ry to approximate the zero-width limit in the calculations of the EPC parameter (λ). The superconducting transition temperature T_c has been estimated with the Allen−Dynes modified McMillan equation[31,32]

$$T_c = \frac{\omega_{\log}}{1.2} \exp\left[\frac{1.04(1 + \lambda)}{\lambda - \mu^* - 0.62\lambda\mu^*}\right] \tag{2}$$

where $\omega_{\log}$ is the logarithmic average frequency and μ^* is the Coulomb pseudopotential, which was taken to be 0.1 (typical value).

The elastic constants (C_{ij}s) of MoB_2 and $Mo_{0.757}B_3$ were obtained with the CASTEP code[33,34] by analyzing stress tensors under small strains. The bulk modulus (K) and shear modulus (G) were thus derived from the Voigt−Reuss−Hill (VRH) approximation,[35] and the Young's modulus (E) and Poisson's ratio (ν) were calculated within the relationship

$$E = \frac{9KG}{3K + G} \tag{3}$$

$$\nu = \frac{6KG}{6K + 2G} \tag{4}$$

RESULTS AND DISCUSSION

Boron-rich metal borides were generally synthesized by mixing metals with excess boron; the residual boron always presents in the synthesized sample, precludes grain growth, and limits our understanding of the intrinsic structure and physical properties. To decrease the reaction temperature and avoid the interference of excess boron, Pt or Bi flux is used to assist the diffusion of refractory Mo and boron, and the temperature gradient method is used in the synthesis, which has been demonstrated to overcome activation barriers and facilitate the rapid formation of transition metal borides under pressure.[3,36,37]

The obtained samples synthesized at 15 GPa via two different heating routes were examined by the back-scattered electron SEM (BSE-SEM), as shown in Figures S3 and S4. The observation reveals a clear phase distribution from MoB_x (MoB_y) to MoB_x (MoB_y) + B and then to Pt + B along the axial direction, which can effectively separate the different borides in the reaction product. EDS analysis (as shown in Table S2) quickly identifies a low-boron MoB_x phase and a high-boron MoB_y phase in the samples obtained at 1650 and 1750 °C, respectively. The samples were further checked by PXRD and SC-XRD. The PXRD pattern (Figure S5a) of low-boron MoB_x was found to have $R\bar{3}m$ (No. 166) symmetry, with the derived lattice parameters (a = 3.012 Å, and c = 20.940 Å) and a unit cell volume of 164.553 Å^3, by Rietveld refinement with the GSAS program. The results match well with both Mo_2B_4 (β-MoB_2) and Mo_2B_5.[16,24,38] Due to the very weak scattering factors of boron, it is hard to locate boron atoms using standard X-ray analysis and hence to identify the difference between Mo_2B_4 and Mo_2B_5 (see Figure S6). Recently, state-of-the-art STEM has enabled atomic-resolution annular bright-field (ABF) imaging of columns of both light and heavy atoms over a wide range of specimen thicknesses.[39−42] The technique was employed to explore the atom structure of low-boron MoB_x. As labeled in Figure S5f, the boron atoms sitting on 3b sites are completely absent in ABF-STEM images along the $[\bar{4}2\bar{1}]$ direction. The synthetic MoB_x with a lower boron concentration is thus indeed Mo_2B_4 (space group $R\bar{3}m$).

The high-boron MoB_y is found to be more stable at higher temperatures compared with low-boron Mo_2B_4. $Mo_{0.8}B_3$ with $P6_3/mmc$ (No. 194) symmetry was used for the Rietveld refinement for MoB_y, yielding the lattice parameters (a = 5.203 Å, and c = 6.357 Å) and a cell volume of 149.071 Å^3, as shown in Figure 1. Compared with stoichiometric MoB_4, boron 4f
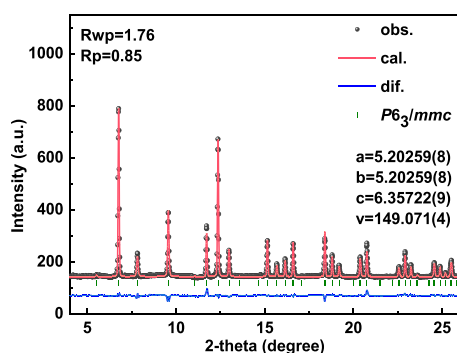
Figure 1. Rietveld refinement of the high-boron MoB_y pattern (as presented in Figure S4c) with the $Mo_{0.8}B_3$ model ($P6_3/mmc$).

sites are fully unoccupied and $2b$ Mo sites (occupancy of 0.6) are partially occupied in $Mo_{0.8}B_3$ (as shown in Table S1). The fully unoccupied $4f$ boron sites result in a two-dimensional distribution in $Mo_{0.8}B_3$ from the three-dimensional arrangement in MoB_4. However, the structure of MoB_y cannot be finalized by the refinement of the PXRD pattern because of the significant similarity of several model XRD patterns (Figure S7). The partial occupancy of Mo1 slightly affects the diffraction intensity of $Mo_{1−x}B_3$, which has a near linear relationship with the intensities of the (100), (002), and (201) planes (Figure S8).

High-quality MoB_y single crystals were selected to precisely understand the location of boron atoms and the occupancy of Mo atoms. The atomic parameters, unit cell information, and fit statistics are listed in Table 1 and Table S3. Single-crystal

Table 1. Atomic Parameters of $Mo_{0.757}B_3$ Determined from SC-XRD Refinement

atom	Mo1	Mo2	B1
site	$2b$	$2c$	$12i$
x	0	1/3	0
y	1	2/3	0.3336(13)
z	0.25	0.25	0
occupancy	0.5139(40)	1	1
U_{iso}*/U_{eq} (Å^2)	0.0026(9)	0.0057(9)	0.0142(57)
U^{11} (Å^2)	0.0033(16)	0.0067(16)	0.0179(78)
U^{22} (Å^2)	0.0033(16)	0.0067(16)	0.0147(72)
U^{33} (Å^2)	0.0011(18)	0.0038(18)	0.0111(95)
U^{12} (Å^2)	0.0017(8)	0.0033(8)	0.0090(39)
U^{13} (Å^2)	0	0	−0.0017(71)
U^{23} (Å^2)	0	0	−0.0008(35)

analysis reveals that there are no boron atoms found in all possible boron positions except for the $12i$ sites, which is consistent with the nonstoichiometric $Mo_{1−x}B_3$ ($x > 0$) models.[15] SC-XRD data also support the incomplete occupancy of Mo1 atoms in $2b$ sites (0, 1, 0.25). The obtained lattice parameters (a = 5.202 Å, and c = 6.356 Å) and the unit cell volume of 148.97 Å^3 from SC-XRD data (Table S3) are consistent with our powder XRD data (Figure 1). As a result, high-boron MoB_y is determined to be $Mo_{0.757}B_3$ with a $P6_3/mmc$ structure having a Mo1 partial occupancy of 0.514, lower than those in $Mo_{0.91}B_3$ (0.82) proposed by Klesnar et al.[23] and $Mo_{0.8}B_3$ (0.6) and $Mo_{3.46}B_{12}$ (0.73) proposed by Lundström et al.[15] Each Mo atom is bonded to the 12 nearest boron atoms and constitutes a head-to-head hexagonal pyramid, as shown in Figure S9 and Table S4. The obtained bond lengths are 2.353

Å for the Mo−B bond and 1.735 Å for the B−B bond, similar to those of the W−B and B−B bonds in $W_{1.094}B_{4.714}$.[4] The shortest B−B distance between the adjacent boron atomic layers was found to be 3.178 Å (Figure S9), which is much larger than the sum of the covalent bond radius (0.82 Å) of two boron atoms. The result indicates the absence of B−B covalent bonding between the (001) boron layers, i.e., two-dimensional distributions of boron atoms in $Mo_{0.757}B_3$.

Figure 2a shows the (average) atomic structure model of $Mo_{0.757}B_3$ projected along the [110] zone axis, with

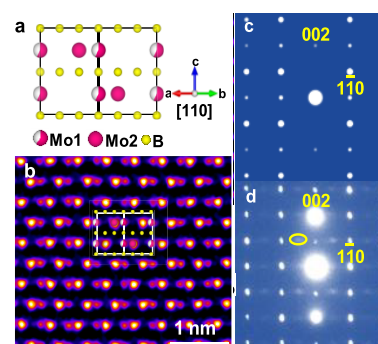**Figure 2.** Crystal structure characterization of $Mo_{0.757}B_3$. (a) Atom structure projection along the [110] zone axis of $Mo_{0.757}B_3$. (b) HAADF image taken along the [110] direction of $Mo_{0.757}B_3$, with the inset showing the atom structure projection along the [110] zone axis of $Mo_{0.757}B_3$. (c) Simulated and (d) experimental selected area electron diffraction patterns obtained from the [110] zone axis.

neighboring individual atom columns of Mo1 ($2b$) and Mo2 ($2c$). Due to the different site occupancies of Mo1 (0.514) and Mo2 (1), the two atom columns show clearly weak and strong contrast in the Z-contrast high-angle annular dark-field (HAADF) image, as shown in Figure 2b. It should be noted that boron atoms can hardly be discerned in the HAADF image due to their weak scattering ability to electrons. Therefore, it seems that the ordered distribution of Mo1 and Mo2 atomic columns is consistent with the average structural model of $Mo_{0.757}B_3$. Compared to the electron diffraction pattern simulated from the average structure model (Figure 2c), however, the experimental selected area electron diffraction (SAED) patterns show additional diffused diffraction spots and a relative intensity difference between the main diffraction spots along [110] (Figure 2d). Note that the latter were taken from a relatively large area (>300 μm^2). The result uncovers the presence of local structural ordering, which was not revealed in the average structural model from XRD measurement, although the local ordering was not observed from the projected HAADF image along the [110] direction.

Interestingly, a local short-range ordering of Mo1 atoms and vacant Mo1 sites was clearly observed along the [201] zone axis of $Mo_{0.757}B_3$. As revealed by the presence of neighboring rather bright and dark atoms shown in the HAADF image (Figure 3a), the ordering occurs by a length scale of 2−10 nm within the (010) planes, with a random distribution within the crystal lattice. Note that the local ordering could be observed only in a rather thin specimen region via high-resolution HAADF imaging. The ordering results in the formation of additional diffused streaks in the corresponding experimental SAED pattern (Figure 3c) as compared to the simulated pattern (Figure 3d). On the basis of the observations, an atom structure model with the local short-range ordering is given in
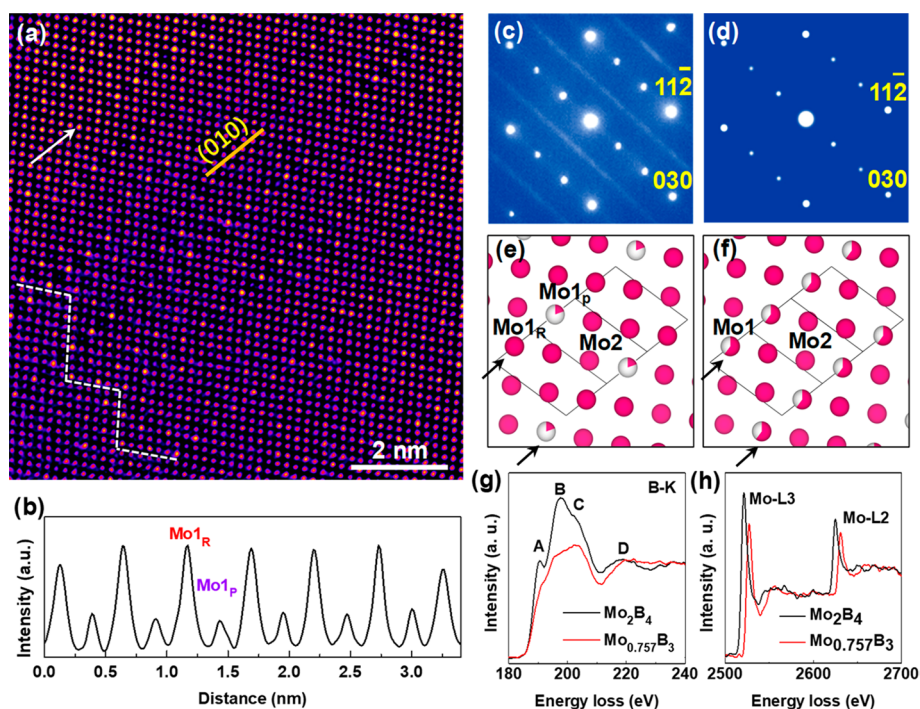
Figure 3. Direct observation of short-range cation (or vacancy) ordering in $Mo_{0.757}B_3$. (a) HAADF image taken along the $[\overline{2}01]$ zone axis of $Mo_{0.757}B_3$ showing the locally short-range ordering of cation (Mo) atoms. The image was processed via the average background subtraction filter (ABSF) method. (b) Intensity-scan file taken from the local (010) plane with short-range ordering of Mo1 atoms, as indicated by the white arrow in panel a. (c) Experimental and (d) simulated selected area electron diffraction patterns obtained from the $[\overline{2}01]$ zone axis. (e) Locally ordered atom and (f) Average atom structure models projected along the same direction. The labels Mo1 and Mo2 represent the Wyckoff $2b$ and $2c$ positions, respectively, in the average crystal structure of $Mo_{0.757}B_3$, while $Mo1_R$ and $Mo1_P$ represent for the locally Mo1-rich and Mo1-poor atom columns, respectively. (g) B-K and (h) Mo-$L_{2,3}$ background-subtracted EELS profiles obtained from the $Mo_{0.757}B_3$ (red) and Mo_2B_4 (black) crystals.

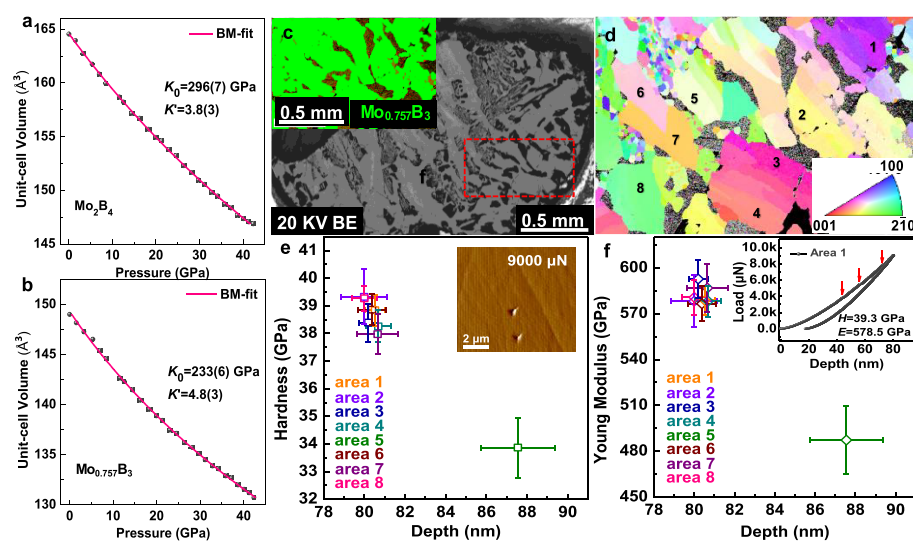**Figure 4.** Characterization of the mechanical properties of $Mo_{0.757}B_3$. (a and b) Pressure dependence of the formula unit volume of Mo_2B_4 and $Mo_{0.757}B_3$ by Rietveld refinements on the XRD patterns. (c) BSE-SEM image of the polished cross section of the synthesized sample at 5 GPa. The inset shows the phase distribution of the area in the red box determined by EBSD. (d) EBSD inverse pole figure (IPF) map of the area marked in panel c. (e and f) Nanoindentation hardness and elastic modulus of areas with different crystallographic orientations numbered in the IPF map. Insets in panels e and f show the atomic force microscopy (AFM) image of indentations under an applied load of 9000 μN and a load–displacement curve for area 1, respectively. The small terrace indicated by the red arrows (in the inset of Figure 4f) may be due to a burst of cracking.

Figure 3e. In contrast to the average crystal structure (Figure 3f) showing a random distribution of Mo atoms and vacancies among the Mo1 sites, the HAADF imaging suggests an alternate presence of Mo1-poor ($Mo1_P$) and Mo1-rich ($Mo1_R$)

columns within the (010) planes. Estimated from the neighboring column contrast difference (Figure 3a), it was found that $Mo1_P$ and $Mo1_R$ columns have site occupancies of roughly 20% and 80%, respectively. Furthermore, The $Mo1_R$–
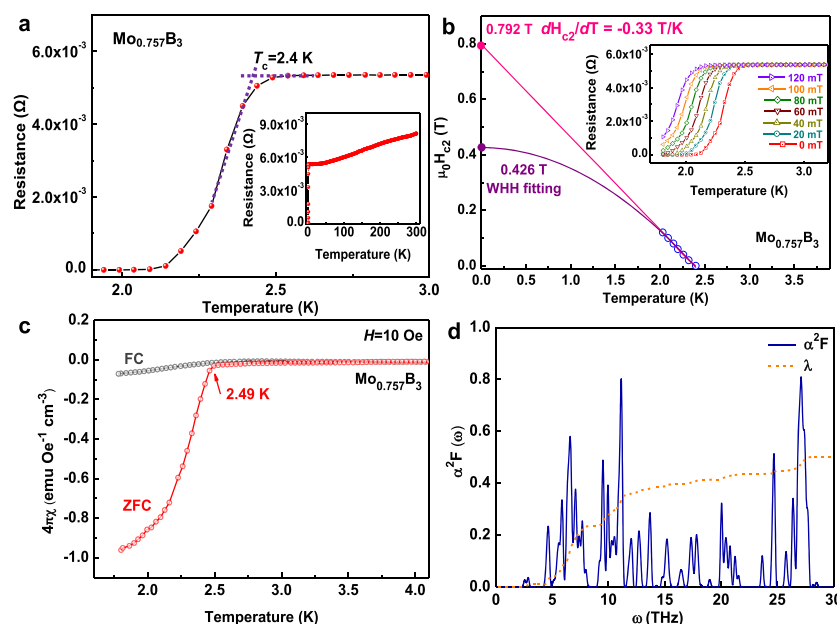
Figure 5. Superconductivity characterization of $Mo_{0.757}B_3$. (a) Temperature-dependent resistance of $Mo_{0.757}B_3$ measured from 1.8 to 3 K. Inset, measured from 1.8 to 300 K. (b) Upper critical field as a function of temperature. Inset, under different magnetic fields, temperature-dependent resistance of $Mo_{0.757}B_3$. (c) Temperature dependence of the volume magnetic susceptibility in an applied magnetic field of 10 Oe. ZFC and FC denote zero-field cooling and field cooling, respectively. (d) Eliashberg EPC spectral function $\alpha^2F(\omega)$ and EPC integration $\lambda(\omega)$ of $Mo_{0.757}B_3$.

$Mo1_R$ distance along the observed direction is twice the Mo2–Mo2 distance. This explains the much brighter contrast of $Mo1_R$ columns than of Mo2 columns. The short-range vacancy ordering observed here also explains the formation of additional diffused streaks as observed in Figure 3c.

Electron energy-loss spectroscopy (EELS) analysis was performed to identify the configuration and coordination states of Mo and B atoms in $Mo_{0.757}B_3$. For this purpose, single-crystal Mo_2B_4 was used as a reference specimen for a comparative study. Compared with the reported B-K edges from varied metal borides,[43] the fine structures of the background-subtracted B-K edges from both the $Mo_{0.757}B_3$ and Mo_2B_4 samples show a 4-fold coordination to Mo atoms (Figure 3g), but the former shows an apparent decrease in the prepeak (B) intensity of the B-K edge, which is consistent with the presence of abundant Mo1 vacancies and hence fewer Mo atoms bonded to each Mo in $Mo_{0.757}B_3$ (Table S5). In addition, the $Mo-L_{2,3}$ from $Mo_{0.757}B_3$ exhibits a decreased peak intensity as well as a red chemical shift compared to that of Mo_2B_4. The difference can be interpreted as a lower concentration as well as a higher valence state of Mo in $Mo_{0.757}B_3$ as compared to Mo_2B_4.

The presence of strong B–B covalent networks and interactions between boron and transition metals is thought to improve the mechanical properties of transition metal borides, e.g., incompressibility and Vickers hardness. The bulk moduli of ReB_2 and OsB_2 (360 and 348 GPa, respectively) are found to be nearly equivalent to that of cubic boron nitride (369 GPa).[5,18,44] The compressibilities of Mo_2B_4 and $Mo_{0.757}B_3$ were investigated by using *in situ* high-pressure synchrotron XRD in a DAC at room temperature. There are no significant changes up to 42 GPa. The bulk modulus (K) and the derivative (K') of the bulk modulus with respect to pressure were obtained by fitting the pressure-dependent volume changes within the three-order Birch–Murnaghan equation of state.[45] The bulk modulus (K_0) of Mo_2B_4 was

determined to be 296 GPa with a K' of 3.8 (Figure 4a), which agrees with the experimental and theoretical bulk moduli (290–310 GPa) of $R\bar{3}m$ MoB_2 (Mo_2B_4).[46,47] However, the K_0 of $Mo_{0.757}B_3$ (233 GPa) is much lower than that of Mo_2B_4 (Figure 4b), which is similar to that of pure boron (224 GPa for β-boron and 227 GPa for B_{28}), Al_2O_3 (252 GPa), and SiC (248 GPa).[44,48−50] The calculations give K_0 values of 296 GPa for Mo_2B_4 and 252 GPa for $Mo_{0.757}B_3$, as listed in Table S6, quite consistent with our experimental results.

To obtain the larger $Mo_{0.757}B_3$ for the characterization of its mechanical behaviors, we further optimize the synthesis process in the following three ways: (1) decreasing the synthesis pressure from 15 to 5 GPa to enhance atomic diffusion, (2) the effect of pressure and temperature control that is tricky for atomic diffusion in borides (thus, the synthesis temperature was increased to 1800 °C), (3) bismuth with a much lower melting point (271 °C) that was used as the flux to enhance the migration of Mo and B atoms in melting bismuth. Figure S10 shows the BSE-SEM images of a sample synthesized at 5 GPa, indicating that the grain sizes of $Mo_{0.757}B_3$ and Mo_2B_4 are up to several hundred micrometers and $Mo_{0.757}B_3$ enriches in a high-temperature area close to bismuth. Figure 4c shows the back-scattered electron SEM image of the cross section of a $Mo_{0.757}B_3$-rich area. The dominant dark gray area represents $Mo_{0.757}B_3$, which was also confirmed by EBSD in the inset of Figure 4c. The obvious difference in the crystallographic orientation is revealed by the EBSD inverse pole figure (IPF) map shown in Figure 4d. The size of $Mo_{0.757}B_3$ single crystals with difference orientations is up to submillimeter dimensions ($\geq$100 μm), allowing us to understand the anisotropic mechanical behavior of $Mo_{0.757}B_3$. The room-temperature nanoindentation experiments with a Berkovich diamond tip were performed for the nano-indentation hardness (H) and Young's modulus (E) (Figure S11). Panels e and f of Figure 4 show the tested hardness and Young's modulus, respectively, of different orientations under

an applied load of 9000 μN, which are also listed in Table S7. The hardness of crystals along the $[12\bar{1}]$ and $[001]$ orientations is found within the range of 38−40 GPa, and the corresponding Young's moduli range from 570 to 590 GPa. The hardness and Young's modulus along the $[\bar{1}4\bar{3}]$ orientation are relatively lower (34 and 480 GPa, respectively). The highest hardness and Young's modulus are similar to those of $WB_{4.2}$.[4] With the decrease in boron concentration, the hardness and Young's modulus are reduced drastically. Mo_2B_4 shows a nanoindentation hardness of 26 GPa and a Young's modulus of 418 GPa (Figure S12), close to the previous reports (21−25 GPa) by Tao et al. and Okada et al.[12,46] For a more comprehensive and reliable characterization, we also carried out the Vickers hardness measurement for $Mo_{0.757}B_3$ along the $[001]$ orientation. As shown in Figure S13, $Mo_{0.757}B_3$ has a gradually stable Vickers hardness of ∼26 GPa under an applied load of 1.96 N, which is lower than that (∼43 GPa) of WB_4 or $WB_{4.2}$ at 0.49 N.[4] Compared with calculated defect-free MoB_3,[20] the calculated bulk modulus, shear modulus, and Young's modulus of $Mo_{0.757}B_3$ are slightly lower than those from experiments (as listed in Table S6), due to the reduced density of covalent bonds caused by Mo vacancies.

Boron-containing compounds usually exhibit high phonon frequencies, which are prone to be conventional electron−phonon coupling superconductors; in particular, MgB_2 and BC_5 have high superconducting temperatures (T_c) of 39 K[51] and 45 K,[52] respectively. Superconductivity is also found in many transition metal borides, such as FeB_4 (2.9 K),[3] ZrB_{12} (5.5 K),[9] and Re_7B_3 (3.3 K).[53] Also, boron-rich $WB_{4.2}$ is reported to have a T_c of 2.05 K.[54] Figure 5a shows the temperature-dependent resistance of $Mo_{0.757}B_3$, indicating a clear superconducting transition of 2.4 K. The resistance−temperature slope dR/dT of $Mo_{0.757}B_3$ shows metallic character, a positive temperature dependence. The inset of Figure 5b indicates the decrease in T_c with an increase in the applied magnetic field from 0 to 120 mT, resulting in the linear temperature-dependent upper critical field (H_{c2}) with an H_{c2}/dT slope of −0.33 T/K (Figure 5b). By the linear extrapolation, the zero-temperature upper critical field (μ_0H_{c2}) is estimated to be 0.792 T. Using the Wert-hammer−Helfand−Hohenberg model,[55] $\mu_0H_{c2}(0)$ is predicted to be 0.426 T. Figure 5c shows the temperature dependence of the volume magnetic susceptibility ($4\pi\chi$) of $Mo_{0.757}B_3$ in an applied magnetic field of 10 Oe. In the zero-field-cooling (ZFC) mode, there is a strong magnetic repulsion, which also reveals the onset temperature of the superconducting transition for $Mo_{0.757}B_3$ is 2.49 K. In addition, the $4\pi\chi$ reflected by the field-cooling (FC) mode is much lower because of the magnetic flux pinning in the process of cooling under magnetic fields. To eliminate the interference of Mo_2B_4 as a possible impurity phase on $Mo_{0.757}B_3$ superconducting properties, we synthesized high-purity Mo_2B_4 at HPHT of 5 GPa, 1500 °C for 30 min, indicated by XRD data in Figure S14 and the measurement of electrical behaviors in range from 1.8 to 300 K (Figure S15). Although Mo_2B_4 has metallic character similar to that of $Mo_{0.757}B_3$, it does not exhibit any superconducting properties above 1.8 K, which is in accordance with the previous report.[56]

Cation vacancy-induced superconductivities were also found in some borides, such as $K_{1−x}B_6$ and $Nb_{1−x}B_2$; in particular, in the Nb−B system, its influence on superconducting properties was studied systematically.[57−59] A deficient occupancy of Nb atoms in $Nb_{1−x}B_2$ leads to the expansion along the c-axis

direction, which in turn weakens Nb−B bonding and enhances the B−B interaction. The emergence of superconductivity is caused by the strong electron−phonon interactions associated with the enhanced B−B bonding. Similarly, the defect-induced lattice expansion along the c-axis direction also presents in $Mo_{0.757}B_3$ (c = 6.3558 Å; c = 6.2891 Å in MoB_3). To understand the origin of superconductivity, we performed the EPC simulations on MoB_3 at ambient pressure. The resulting total λ of 0.2 is rather small, indicating the weak EPC in MoB_3, and it is unlikely to become a superconductive phase. To the best of our knowledge, proper defects in materials are expected to modify the electronic structure. Thus, we performed EPC simulation to check the possible superconductivity in $Mo_{0.757}B_3$. The estimated T_c is around 8 K with a λ of 0.55 by the use of the Allen−Dynes modified McMillan equation. The Eliashberg EPC spectral function $\alpha^2F(\omega)$ and EPC integration $\lambda(\omega)$ of $Mo_{0.757}B_3$ are plotted in Figure 5d. The calculated results confirm the central role of vacancy in superconducting $Mo_{0.757}B_3$.

CONCLUSIONS

In summary, under HPHT conditions, we report a successful synthesis of highest boron molybdenum boride. The structure and composition were finally determined to be $Mo_{0.757}B_3$ with $P6_3/mmc$ symmetry having a partial occupancy of 0.514 in $2b$ Mo sites by SC-XRD and STEM analysis. These Mo vacancies exhibit short-range ordering on the (010) planes. The $Mo_{0.757}B_3$ shows excellent mechanical properties, including a high bulk modulus of 233 GPa, an anisotropic nanoindentation hardness of ∼34−40 GPa, and a Young's modulus range from 480 to 590 GPa in different crystal orientations. In particular, the hardness of crystals near $[001]$ and $[2\bar{1}0]$ orientations is found from 38 to 40 GPa, and the corresponding Young's modulus ranges from 570 to 590 GPa. Meanwhile, the resistance and magnetic measurements indicate that $Mo_{0.757}B_3$ is superconducting with a T_c of 2.4 K. Theoretical calculations reveal that the superconducting properties are due to the partial occupancy of Mo atoms.

ASSOCIATED CONTENT

ⓢ Supporting Information

The Supporting Information is available free of charge at https://pubs.acs.org/doi/10.1021/acs.chemmater.9b04052.

Summary of previous highest boron MoB_y models (Table S1), elemental analysis of high-purty MoB_x and MoB_y areas (Table S2), unit cell information about $Mo_{0.757}B_3$ and fit statistics from SC-XRD refinement (Table S3), refined atomic spacings (angstroms) in $Mo_{0.757}B_3$ (Table S4), details for coordination of Mo and B atoms in phases of Mo_2B_4 and $Mo_{0.757}B_3$ (Table S5), calculated properties of Mo_2B_4 and $Mo_{0.757}B_3$ (Table S6), nanoindentation hardness and elastic modulus of $Mo_{0.757}B_3$ with different crystallographic orientations (Table S7), assembly schematics for high-temperature and high-pressure experiments (Figures S1 and S2), BSE-SEM images of samples (Figures S3 and S4), XRD and TEM results of Mo_2B_4 (Figures S5 and S6), XRD patterns of experimental and simulated high-boron MoB_y (Figures S7 and S8), details for coordination of Mo and B atoms in $Mo_{0.757}B_3$ (Figure S9), micro-structures and mechanical properties of $Mo_{0.757}B_3$ (Figures S10−S13), and XRD patterns of temperature-

dependent resistance of Mo_2B_4 (Figures S14 and S15) (PDF)

■ AUTHOR INFORMATION

Corresponding Author
*E-mail: huiyang.gou@hpstar.ac.cn.

ORCID ⊙
Dongzhou Zhang: 0000-0002-6679-892X
Hanyu Liu: 0000-0003-2394-5421
Faming Gao: 0000-0001-8711-7153
Rajeev Ahuja: 0000-0003-1231-9994
Huiyang Gou: 0000-0002-2612-4314

Author Contributions
■H.T., X.G., and J.Z. contributed equally to this work.

Notes
The authors declare no competing financial interest.

■ REFERENCES

(1) Chung, H. Y.; Weinberger, M. B.; Levine, J. B.; Kavner, A.; Yang, J. M.; Tolbert, S. H.; Kaner, R. B. Synthesis of Ultra-Incompressible Superhard Rhenium Diboride at Ambient Pressure. *Science* **2007**, *316* (5823), 436−439.

(2) Akopov, G.; Yeung, M. T.; Turner, C. L.; Mohammadi, R.; Kaner, R. B. Extrinsic Hardening of Superhard Tungsten Tetraboride Alloys with Group 4 Transition Metals. *J. Am. Chem. Soc.* **2016**, *138* (17), 5714−5721.

(3) Gou, H.; Dubrovinskaia, N.; Bykova, E.; Tsirlin, A. A.; Kasinathan, D.; Schnelle, W.; Richter, A.; Merlini, M.; Hanfland, M.; Abakumov, A. M.; Batuk, D.; Van Tendeloo, G.; Nakajima, Y.; Kolmogorov, A. N.; Dubrovinsky, L. Discovery of a Superhard Iron Tetraboride Superconductor. *Phys. Rev. Lett.* **2013**, *111* (15), 157002.

(4) Lech, A. T.; Turner, C. L.; Mohammadi, R.; Tolbert, S. H.; Kaner, R. B. Structure of Superhard Tungsten Tetraboride: A Missing Link between MB_2 and MB_{12} Higher Borides. *Proc. Natl. Acad. Sci. U. S. A.* **2015**, *112* (11), 3223−3228.

(5) Gu, Q.; Krauss, G.; Steurer, W. Transition Metal Borides: Superhard versus Ultra-Incompressible. *Adv. Mater.* **2008**, *20* (19), 3620−3626.

(6) Tao, Q.; Cui, T.; Feng, X.; Chen, Y.; Wang, X.; Zhu, P.; Zheng, W.; Lian, M.; Xu, C.; Li, L. Modulating Hardness in Molybdenum Monoborides by Adjusting an Array of Boron Zigzag Chains. *Chem. Mater.* **2019**, *31* (1), 200−206.

(7) Mohammadi, R.; Xie, M.; Lech, A. T.; Turner, C. L.; Kavner, A.; Tolbert, S. H.; Kaner, R. B. Toward Inexpensive Superhard Materials: Tungsten Tetraboride-Based Solid Solutions. *J. Am. Chem. Soc.* **2012**, *134* (51), 20660−20668.

(8) Akopov, G.; Roh, I.; Sobell, Z. C.; Yeung, M. T.; Pangilinan, L.; Turner, C. L.; Kaner, R. B. Effects of Variable Boron Concentration on the Properties of Superhard Tungsten Tetraboride. *J. Am. Chem. Soc.* **2017**, *139* (47), 17120−17127.

(9) Ma, T.; Li, H.; Zheng, X.; Wang, S.; Wang, X.; Zhao, H.; Han, S.; Liu, J.; Zhang, R.; Zhu, P.; Long, Y.; Cheng, J.; Ma, Y.; Zhao, Y.; Jin, C.; Yu, X. Ultrastrong Boron Frameworks in ZrB_{12}: A Highway for Electron Conducting. *Adv. Mater.* **2017**, *29* (3), 1604003.

(10) Chen, Y.; Yu, G.; Chen, W.; Liu, Y.; Li, G. D.; Zhu, P.; Tao, Q.; Li, Q.; Liu, J.; Shen, X.; Li, H.; Huang, X.; Wang, D.; Asefa, T.; Zou, X. Highly Active, Nonprecious Electrocatalyst Comprising Borophene Subunits for the Hydrogen Evolution Reaction. *J. Am. Chem. Soc.* **2017**, *139* (36), 12370−12373.

(11) Zhang, R. F.; Legut, D.; Lin, Z. J.; Zhao, Y. S.; Mao, H. K.; Veprek, S. Stability and Strength of Transition-Metal Tetrabordes and Tribordes. *Phys. Rev. Lett.* **2012**, *108* (25), 25502.

(12) Okada, S.; Atoda, T.; Higashi, I.; Takahashi, Y. Preparation of Single Crystals of MoB_2 by the Aluminium-Flux Technique and Some of Their Properties. *J. Mater. Sci.* **1987**, *22* (8), 2993−2999.

(13) Li, Q.; Zhou, D.; Zheng, W.; Ma, Y.; Chen, C. Global Structural Optimization of Tungsten Borides. *Phys. Rev. Lett.* **2013**, *110* (13), 136403.

(14) Zhang, M.; Wang, H.; Wang, H.; Cui, T.; Ma, Y. Structural Modifications and Mechanical Properties of Molybdenum Borides from First Principles. *J. Phys. Chem. C* **2010**, *114* (14), 6722−6725.

(15) Lundström, T.; Rosenberg, I. The Crystal Structure of the Molybdenum Boride $Mo_{1-x}B_3$. *J. Solid State Chem.* **1973**, *6* (2), 299−305.

(16) Frotscher, M.; Klein, W.; Bauer, J.; Fang, C.-M.; Halet, J.-F.; Senyshyn, A.; Baehtz, C.; Albert, B. M_2B_5 or M_2B_4? A Reinvestigation of the Mo/B and W/B System. *Z. Anorg. Allg. Chem.* **2007**, *633* (15), 2626−2630.

(17) Spear, K. E.; Liao, P. K. The B-Mo (Boron-Molybdenum) System. *Bull. Alloy Phase Diagrams* **1988**, *9* (4), 457−466.

(18) Levine, J. B.; Tolbert, S. H.; Kaner, R. B. Advancements in the Search for Superhard Ultra-Incompressible Metal Borides. *Adv. Funct. Mater.* **2009**, *19* (22), 3519−3533.

(19) Mohammadi, R.; Lech, A. T.; Xie, M.; Weaver, B. E.; Yeung, M. T.; Tolbert, S. H.; Kaner, R. B. Tungsten Tetraboride, an Inexpensive Superhard Material. *Proc. Natl. Acad. Sci. U. S. A.* **2011**, *108* (27), 10958−10962.

(20) Liang, Y.; Yuan, X.; Fu, Z.; Li, Y.; Zhong, Z. An Unusual Variation of Stability and Hardness in Molybdenum Borides. *Appl. Phys. Lett.* **2012**, *101* (18), 181908.

(21) Shein, I. R.; Shein, K. I.; Ivanovskii, A. L. First-Principles Study on the Structural, Cohesive and Electronic Properties of Rhombohedral Mo_2B_5 as Compared with Hexagonal MoB_2. *Phys. B* **2007**, *387* (1−2), 184−189.

(22) Kiessling, R.; Wetterholm, A.; Sillen, L. G.; Linnasalmi, A.; Laukkanen, P. The Crystal Structures of Molybdenum and Tungsten Borides. *Acta Chem. Scand.* **1947**, *1*, 893−916.

(23) Klesnar, H.; Aselage, T. L.; Morosin, B.; Kwei, G. H. The Diboride Compounds of Molybdenum: MoB_{2-x} and Mo_2B_{5-y}. *J. Alloys Compd.* **1996**, *241* (1−2), 180−186.

(24) Higashi, I.; Takahashi, Y.; Okada, S. Crystal Structure of MoB_2. *J. Less-Common Met.* **1986**, *123* (1−2), 277−283.

(25) Nowotny, H.; Haschke, H.; Benesovsky, F. Bor-Reiche Wolframboride. *Monatsh. Chem.* **1967**, *98* (3), 547−554.

(26) Petrícek, V.; Dušek, M.; Palatinus, L. Crystallographic Computing System JANA2006: General Features. *Z. Kristallogr. - Cryst. Mater.* **2014**, *229* (5), 345−352.

(27) Zhang, D.; Dera, P. K.; Eng, P. J.; Stubbs, J. E.; Zhang, J. S.; Prakapenka, V. B.; Rivers, M. L. High Pressure Single Crystal Diffraction at PX̂2. *J. Visualized Exp.* **2017**, 54660.

(28) Prescher, C.; Prakapenka, V. B. DIOPTAS: A Program for Reduction of Two-Dimensional X-Ray Diffraction Data and Data Exploration. *High Pressure Res.* **2015**, *35* (3), 223−230.

(29) Toby, B. H. EXPGUI, a Graphical User Interface for GSAS. *J. Appl. Crystallogr.* **2001**, *34* (2), 210−213.

(30) Giannozzi, P.; Baroni, S.; Bonini, N.; Calandra, M.; Car, R.; Cavazzoni, C.; Ceresoli, D.; Chiarotti, G. L.; Cococcioni, M.; Dabo, I.; Dal Corso, A.; de Gironcoli, S.; Fabris, S.; Fratesi, G.; Gebauer, R.; Gerstmann, U.; Gougoussis, C.; Kokalj, A.; Lazzeri, M.; Martin-Samos, L.; Marzari, N.; Mauri, F.; Mazzarello, R.; Paolini, S.; Pasquarello, A.; Paulatto, L.; Sbraccia, C.; Scandolo, S.; Sclauzero, G.; Seitsonen, A. P.; Smogunov, A.; Umari, P.; Wentzcovitch, R. M. QUANTUM ESPRESSO: A Modular and Open-Source Software Project for Quantum Simulations of Materials. *J. Phys.: Condens. Matter* **2009**, *21* (39), 395502.

(31) Dynes, R. C. McMillan's Equation and the Tc of Super-conductors. *Solid State Commun.* **1972**, *10* (7), 615−618.

(32) Allen, P. B.; Dynes, R. C. Transition Temperature of Strong-Coupled Superconductors Reanalyzed. *Phys. Rev. B* **1975**, *12* (3), 905−922.

(33) Wang, Y.; Lv, J.; Zhu, L.; Ma, Y. Crystal Structure Prediction via Particle-Swarm Optimization. *Phys. Rev. B: Condens. Matter Mater. Phys.* **2010**, *82* (9), 094116.

(34) Wang, Y.; Lv, J.; Zhu, L.; Ma, Y. CALYPSO: A Method for Crystal Structure Prediction. *Comput. Phys. Commun.* **2012**, *183* (10), 2063−2070.

(35) Hill, R. The Elastic Behaviour of a Crystalline Aggregate. *Proc. Phys. Soc., London, Sect. A* **1952**, *65* (5), 349−354.

(36) Gou, H.; Tsirlin, A. A.; Bykova, E.; Abakumov, A. M.; Van Tendeloo, G.; Richter, A.; Ovsyannikov, S. V.; Kurnosov, A. V.; Trots, D. M.; Konôpková, Z.; Liermann, H.-P.; Dubrovinsky, L.; Dubrovinskaia, N. Peierls Distortion, Magnetism, and High Hardness of Manganese Tetraboride. *Phys. Rev. B: Condens. Matter Mater. Phys.* **2014**, *89* (6), 064108.

(37) Bykova, E.; Tsirlin, A. A.; Gou, H.; Dubrovinsky, L.; Dubrovinskaia, N. Novel Non-Magnetic Hard Boride Co_5B_{16} Synthesized under High Pressure. *J. Alloys Compd.* **2014**, *608*, 69−72.

(38) Kudaka, K.; Iizumi, K.; Sasaki, T.; Okada, S. Mechanochemical Synthesis of MoB_2 and Mo_2B_5. *J. Alloys Compd.* **2001**, *315* (1−2), 104−107.

(39) Findlay, S. D.; Shibata, N.; Sawada, H.; Okunishi, E.; Kondo, Y.; Ikuhara, Y. Dynamics of Annular Bright Field Imaging in Scanning Transmission Electron Microscopy. *Ultramicroscopy* **2010**, *110* (7), 903−923.

(40) Gao, X.; Fisher, C. A. J.; Kimura, T.; Ikuhara, Y. H.; Moriwake, H.; Kuwabara, A.; Oki, H.; Tojigamori, T.; Huang, R.; Ikuhara, Y. Lithium Atom and A-Site Vacancy Distributions in Lanthanum Lithium Titanate. *Chem. Mater.* **2013**, *25* (9), 1607−1614.

(41) Gao, X.; Ikuhara, Y. H.; Fisher, C. A. J.; Moriwake, H.; Kuwabara, A.; Oki, H.; Kohama, K.; Yoshida, R.; Huang, R.; Ikuhara, Y. Structural Distortion and Compositional Gradients Adjacent to Epitaxial $LiMn_2O_4$ Thin Film Interfaces. *Adv. Mater. Interfaces* **2014**, *1* (8), 1400143.

(42) Gao, X.; Fisher, C. A. J.; Ikuhara, Y. H.; Fujiwara, Y.; Kobayashi, S.; Moriwake, H.; Kuwabara, A.; Hoshikawa, K.; Kohama, K.; Iba, H.; Ikuhara, Y. Cation Ordering in A-Site-Deficient Li-Ion Conducting Perovskites $La_{(1-x)/3}Li_xNbO_3$. *J. Mater. Chem. A* **2015**, *3* (7), 3351−3359.

(43) Garvie, L. A. J.; Craven, A. J.; Brydson, R. Parallel Electron Energy-Loss Spectroscopy (PEELS) Study of B in Minerals; the Electron Energy-Loss near-Edge Structure (ELNES) of the B K Edge. *Am. Mineral.* **1995**, *80* (11−12), 1132−1144.

(44) Léger, J. M.; Haines, J.; Schmidt, M.; Petitet, J. P.; Pereira, A. S.; da Jornada, J. A. H. Discovery of Hardest Known Oxide. *Nature* **1996**, *383* (6599), 401−401.

(45) Birch, F. Finite Elastic Strain of Cubic Crystals. *Phys. Rev.* **1947**, *71* (11), 809−824.

(46) Tao, Q.; Zhao, X.; Chen, Y.; Li, J.; Li, Q.; Ma, Y.; Li, J.; Cui, T.; Zhu, P.; Wang, X. Enhanced Vickers Hardness by Quasi-3D Boron Network in MoB_2. *RSC Adv.* **2013**, *3* (40), 18317−18322.

(47) Liu, P.; Peng, F.; Yin, S.; Liu, F.; Wang, Q.; Zhu, X.; Wang, P.; Liu, J.; He, D. Exploring the Behavior of Molybdenum Diboride (MoB_2): A High Pressure x-Ray Diffraction Study. *J. Appl. Phys.* **2014**, *115* (16), 163502.

(48) Hamel, G.; Allan, D. R.; Grima, P.; Loveday, J. S.; Nelmes, R. J.; Besson, J. M.; Hull, S. Neutron- and x-Ray-Diffraction Measurements of the Bulk Modulus of Boron. *Phys. Rev. B: Condens. Matter Mater. Phys.* **1993**, *47* (13), 7668−7673.

(49) Zarechnaya, E. Y.; Dubrovinsky, L.; Dubrovinskaia, N.; Filinchuk, Y.; Chernyshov, D.; Dmitriev, V.; Miyajima, N.; El Goresy, A.; Braun, H. F.; Van Smaalen, S.; Kantor, I.; Kantor, A.; Prakapenka, V.; Hanfland, M.; Mikhaylushkin, A. S.; Abrikosov, I. A.; Simak, S. I. Superhard Semiconducting Optically Transparent High Pressure Phase of Boron. *Phys. Rev. Lett.* **2009**, *102* (18), 185501.

(50) Sung, C. M.; Sung, M. Carbon Nitride and Other Speculative Superhard Materials. *Mater. Chem. Phys.* **1996**, *43* (1), 1−18.

(51) Nagamatsu, J.; Nakagawa, N.; Muranaka, T.; Zenitani, Y.; Akimitsu, J. Superconductivity at 39 K in Magnesium Diboride. *Nature* **2001**, *410* (6824), 63−64.

(52) Calandra, M.; Mauri, F. High-Tc superconductivity in superhard diamondlike BC_5. *Phys. Rev. Lett.* **2008**, *101* (1), 016401.

(53) Kawano, A.; Mizuta, Y.; Takagiwa, H.; Muranaka, T.; Akimitsu, J. The Superconductivity in Re-B System. *J. Phys. Soc. Jpn.* **2003**, *72* (7), 1724−1728.

(54) Carnicom, E. M.; Strychalska-Nowak, J.; Wiśniewski, P.; Kaczorowski, D.; Xie, W.; Klimczuk, T.; Cava, R. J. Superconductivity in the Superhard Boride $WB_{4.2}$. *Supercond. Sci. Technol.* **2018**, *31* (11), 115005.

(55) Helfand, E.; Werthamer, N. R. Temperature and purity dependence of the superconducting critical field, Hc2. *Phys. Rev. Lett.* **1964**, *13* (23), 686−688.

(56) Muzzy, L.; Avdeev, M.; Lawes, G.; Haas, M.; Zandbergen, H.; Ramirez, A.; Jorgensen, J.; Cava, R. Structure and Superconductivity in Zr-Stabilized, Nonstoichiometric Molybdenum Diboride. *Phys. C* **2002**, *382* (2−3), 153−165.

(57) Miao, R.; Bai, Z.; Liu, C.; Wu, F.; Zhang, X.; Wang, H.; Yang, J. Potentially High-Temperature Superconductivity in $K_{1-x}B_6$: A First-Principles Prediction. *Phys. C* **2018**, *551*, 16−18.

(58) Ren, Z.; Kuroiwa, S.; Tomita, Y.; Akimitsu, J. Structural Phase Evolution and Superconductivity in the Non-Stoichiometric Inter-metallic Compound Niobium Diboride. *Phys. C* **2008**, *468* (5), 411−416.

(59) Mudgel, M.; Awana, V. P. S.; Kishan, H.; Felner, I.; Alvarez, D. G. A.; Bhalla, G. L. Superconductivity of Various Borides: The Role of Stretched c-Parameter. *J. Appl. Phys.* **2009**, *105* (7), 07E313.